# Failure Mechanisms at Interfaces between Lithium Metal Electrodes and a Single-ion Conducting Polymer Gel Electrolyte

Louise Frenck<sup> $a,b,\dagger$ </sup>, Peter Lennartz<sup> $c,d,\dagger$ </sup>, Dilworth Y. Parkinson<sup>e</sup>, Martin Winter<sup>c,f</sup>, Nitash P. Balsara<sup>a,b,\*</sup>, Gunther Brunklaus<sup>c,\*</sup>

<sup>a</sup>Department of Chemical and Biomolecular Engineering, University of California, Berkeley, California 94720, United States

<sup>b</sup>Materials Sciences Division, Lawrence Berkeley National Laboratory, Berkeley, California 94720, United States

<sup>c</sup>Forschungszentrum Jülich GmbH, Helmholtz-Institute Münster (IEK-12), Corrensstr. 46, 48149 Münster, Germany

<sup>d</sup>University of Duisburg-Essen, Faculty of Physics, Lotharstr. 1-21, 47048 Duisburg, Germany

<sup>e</sup>Advanced Light Source, Lawrence Berkeley National Laboratory, Berkeley, California 94720, United States

<sup>f</sup>University of Münster, MEET Battery Research Center, Institute of Physical Chemistry, Corrensstr. 46, 48149 Münster, Germany

†Contributed equally to this work

\*Corresponding authors: g.brunklaus@fz-juelich.de; nbalsara@berkeley.edu

KEYWORDS: "Lithium Metal", Single Ion Conductor", "Polymer Electrolyte", "X-Ray Microtomography", "Electrochemical Impedance Spectroscopy"

#### **ABSTRACT**

Polymer electrolytes have the potential to enable rechargeable lithium (Li) metal batteries. However, growth of non-uniform high surface area Li still occurs frequently and eventually leads to a short circuit. In this study, a single-ion conducting polymer gel electrolyte is operated at room temperature in symmetric Li||Li cells. We use X-Ray microtomography and electrochemical impedance spectroscopy (EIS) to study the cells. In separate experiments, cells were cycled at current densities of 0.1 mA cm<sup>-2</sup> and 0.3 mA cm<sup>-2</sup>, and short circuits were obtained eventually after an average of approximately 240 cycles and 30 cycles, respectively. EIS reveals an initially decreasing interfacial resistance associated with electrodeposition of nonuniform Li protrusions and the concomitant increase in electrode surface area. X-Ray microtomography images show that many of the nonuniform Li deposits at 0.1 mA cm<sup>-2</sup> are related to the presence of impurities in both electrolyte and electrode phases. Protrusions are globular when they are close to electrolyte impurities but are moss-like when they appear near the impurities in the lithium metal. At long times, the interfacial resistance increases, perhaps due to additional impedance due the formation of additional solid electrolyte interface (SEI) at the growing protrusions until the cells short. At 0.3 mA cm<sup>-2</sup>, large regions of the electrode-electrolyte interface are covered with mossy deposits. EIS reveals a decreasing interfacial resistance due to the increase in interfacial area up to short circuit; the increase in interfacial impedance observed at the low current density is not observed. The results emphasize the importance of pure surfaces and materials on the microscopic scale and suggest modification of interfaces and electrolyte may be necessary to enable uniform Li electrodeposition at high current densities.

#### INTRODUCTION

Increasing demand for high-energy density rechargeable batteries has led to a substantial progress in the development of beyond lithium-ion battery technologies. The commercial utilization of lithium (Li) metal as anode material is one strategy to drastically increase energy density. However, these batteries exhibit limited reversibility and reduced cycle life due to the instability of interfaces between the anode and electrolyte [1-4]. Inhomogeneous Li plating and stripping may lead to the formation of high-surface area Li [5] deposits, which can occur in different morphologies where dendrites, globules or mossy structures are prominent examples [6]. In this respect, polymer electrolytes constitute a promising class of materials for Li metal batteries, as they can potentially hinder the formation of high surface area deposits [7-11]. Dry polymer electrolytes can only support high current densities needed for practical applications at elevated temperatures. Room temperature operation is, however, enabled in polymer gel electrolytes with added solvents [8]. Included in this class of electrolytes are single-ion conducting gels [12-14]. The immobilization of anions has the advantage of reducing polarization during cell operation, which lowers the risk of anion depletion at the interface and associated dendritic growth of Li [15]. Though many materials that withstand prolonged cycling have been suggested [16], many questions concerning underlying failure mechanisms remain unresolved. Non-destructive characterization techniques are particularly relevant for answering these questions [17]. Examples of advanced characterization methods are in-situ optical microscopy [18,19], in-situ XPS [20] and TOF-SIMS [21], as well as cryogenic electron microscopy [22,23]. In contrast to the limited resolution and depth of field of optical methods and partly cumbersome sample preparation, X-Ray microtomography allows for reconstruction of an optical image throughout the whole depth of the sample without having to disassemble the cell. In principal, a sealed pouch cell is illuminated with monochromatic X-Rays and an optical image is reconstructed from the radiogram using a scintillator and an optical

microscope [24]. Hard X-Ray microtomography has been used to study the interface between Li and polymer electrolytes, and to monitor the morphological changes upon Li plating and stripping [6,7,14,25-31]. The cycling experiments in these studies were conducted at temperatures well above room temperature (*e.g.*, 90 °C). We are only aware of one X-Ray microtomography study of single-ion conducting gels [14]. Electrochemical impedance spectroscopy is another powerful non-destructive method to investigate interfacial changes upon cell operation [32-35]. However, the relationship between interfacial resistance measured by impedance spectroscopy and the morphology of Li deposits is often unclear.

In this work, the stability of a single-ion conducting gel polymer electrolyte is studied in symmetric Li||Li cells. The evolution of the interfaces between the Li metal electrode and electrolyte is monitored by *in situ* X-Ray microtomography and electrochemical impedance spectroscopy. A variety of Li deposits nucleate and grow during cycling, revealing strong correlations between the nature of the deposits and impurities in both Li metal and the electrolyte. The nature of the deposits changes qualitatively when the current density is increased from 0.1 mA cm<sup>-2</sup> to 0.3 mA cm<sup>-2</sup>. Correlations between the X-Ray microtomography and electrochemical impedance spectroscopy data, or lack thereof, is discussed.

# **METHODS**

### Materials

A negatively charged polysulfonamide (PSA) with mobile Li<sup>+</sup> counter-ions (**Figure 1**) was synthesized following an established and previously published protocol [12]. Flexible membranes were obtained by blending PSA with poly(vinylidene fluoride-co-hexafluoropropylene) (PVDF-HFP) in a weight ratio of 1:3 (PVDF-HFP: PSA). 100 mg of PVDF-HFP were dissolved in 4 mL of anhydrous n-methyl-2-pyrrolidone (NMP) and 300 mg of PSA was added subsequently. The

solution was stirred overnight at 60 °C to obtain a homogeneous solution. For membrane casting, the solution was poured into an evaporation dish and dried in a vacuum oven at 80 °C for 24 h. The resulting membrane was swollen with a mixture of ethylene carbonate (EC) and propylene carbonate (PC) (EC:PC ratio of 1:1 vol.) and equilibrated overnight in a dry-room with reduced humidity (< 20 ppm H<sub>2</sub>O) before sealing it between two mylar foils in a pouch bag for storage and shipping (Note that all polymer films were made in Münster).

# 

Figure 1. Molecular structure (a) and picture of the single-ion conducting polymer electrolyte (b). The flexible membrane is achieved by blending the polymer with PVDF-HFP (1:3 blender:polymer ratio by weight) and swelling it with a mixture of EC:PC solvent (130 wt %). Synthesis and fabrication procedure are similar to previously published work [12].

Previous work on this gel polymer demonstrated that it is an electrolyte with a transference number of 0.9 and bulk ionic conductivity (measured with blocking electrodes) of 0.5 mS cm<sup>-1</sup> at 20 °C

[13,14,36,37]. The solvent uptake in the gel amounts to approximately 130% the weight of the dry film [12].

#### Symmetric lithium-electrolyte-lithium cell assembly

All electrolyte preparation and electrochemical cell assembly steps were performed in Berkeley in argon-filled gloveboxes with less than 1 ppm of water as well as less than 1 ppm of oxygen to avoid contamination. Casted membranes shipped from Münster to Berkeley were soaked again in the EC:PC mixture described above, to ensure complete wetting and reverse changes that might have occurred during shipping; this soaking was necessary to achieve reproducible results. We expect the solvent uptake to be about 130 wt%, which is the natural limit of this material [12]. The solventcontaining films were cut using a 11.43 mm diameter metal punch to obtain a gel electrolyte disc. Li metal foils with 99.99% purity and a thickness of 250 µm (Honjo) were used to prepare symmetric Li-electrolyte-Li cells. In order to prepare the cells, a nickel foil was used as current collector and three layers of Li metal foil were stacked on top of it. The assembled electrode was then pressed inside a polypropylene-lined-aluminum pouch material with a pneumatic press at 130 MPa - the electrode appeared flat and shiny after this step. The Li-Nickel metal electrodes were made by cutting the three layers of Li foil and nickel foil backing using a 9.525 mm metal punch to obtain disc electrodes. The electrolyte film was sandwiched between two disc electrodes. In order to keep the cell horizontal during tomography, two 0.25 mm thick stainless-steel shims were added above and beneath the cell. Aluminum current collector tabs were affixed to the stainless-steel shims, and the whole assembly was vacuum sealed in a polypropylene-lined-aluminum pouch material in order to conduct experiments outside the glovebox. A schematic of the cell stack can be found in the Supporting Information (Figure S1).

# Cycling experiments

All cycling experiments were run at 25 °C inside an environmental chamber (MACCOR). All the cells were equilibrated for 6 h at this temperature before commencing cycling experiments. Cells were galvanostatically conditioned, using a BioLogic VMP3 potentiostat, at a low current density of i = 0.02 mA cm<sup>-2</sup> for 10 cycles. One cycle consists of 4h polarization applying a positive current, followed by 45 min of rest; and 4h polarization applying a negative current followed by 45 min of rest. The first batch of cells was galvanostatically cycled at a current density of i = 0.1 mA cm<sup>-2</sup> (corresponding to ~2 µm of Li per half-cycle, or 0.1 mg cm<sup>-2</sup>) while a second batch of cells was galvanostatically cycled at a current density of i = 0.3 mA cm<sup>-2</sup> (~6 µm of Li, or 0.3 mg cm<sup>-2</sup>). Apart from the current density, the cycling procedure was the same as for conditioning cycles. After each cycle following the 45 min of rest, electrochemical impedance spectra were acquired using a BioLogic VMP3 with a frequency range from 1 MHz to 0.1 Hz at an amplitude of 40 mV. The data was analyzed by fitting a distribution of relaxation times (DRT) to the measured impedances and identifying trends in the time domain, as well as in the Nyquist plot. Kramers-Kronig conformity tests were performed to ensure validity and stationarity of the system during the time of the measurement. Integration of the DRT intensity was performed to determine the interfacial resistances.

# DRT analysis

Distribution of relaxation times (DRT) analysis [38,39] of measured impedance spectra was performed using a custom-made script in Wolfram Mathematica software. The model used in the DRT script contains a single resistor (modeling bulk resistance) in series with a large number of RC-elements (resistor and capacitor in parallel, characterized by the time constant  $\tau = RC$ ), modelling similar but not equal processes and interphases. Note that the RC-elements account for charge separation layers (polarization) and charge transfer across the layers. The data is fitted by

non-linear least square minimization including an optimized regularization parameter of  $\lambda=0.1$ , which acts as an additional constraint in the minimization problem and reduces the sensitivity towards noise (in other words,  $\lambda$  acts as 'dwell time' with which the data is sampled in the frequency domain). As DRT analysis is sensitive to noise and boundary points, measured points within a smaller frequency range of 14.4 kHz - 1.27 Hz were considered for all the spectra. Further details of the DRT algorithm are provided in the Supporting Information.

# Hard X-ray microtomography

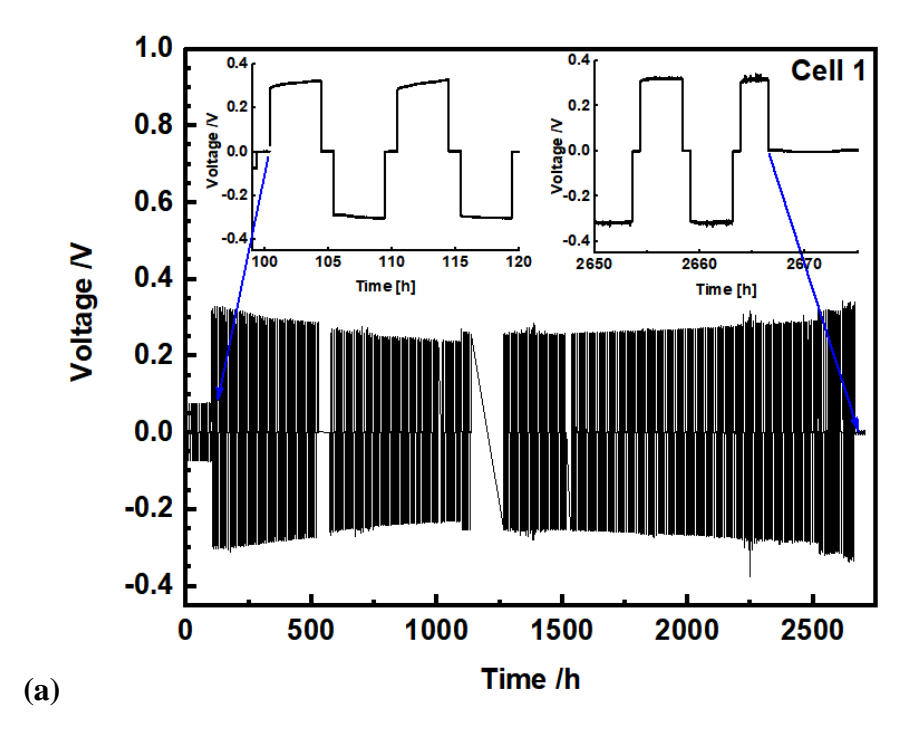
Cells run at a current density of i=0.1 mA cm<sup>-2</sup> were stopped and removed from the environmental chamber to allow imaging of the cells using hard X-ray microtomography after conditioning, after 40 cycles, after 87 cycles, and after failure. For the cells operated at i=0.3 mA cm<sup>-2</sup>, cells were imaged after conditioning cycles and after failure which occurred after relatively few cycles. Monochromatic hard X-rays with energy of 22 keV were used at beamline 8.3.2 at the Advanced Light Source (ALS) at the Lawrence Berkeley National Laboratory (LBNL). Cells were illuminated and the X-ray shadow casted by the sample was converted into visible light using a scintillator. An optical microscope magnified this image and converted it into a digital image file (a schematic can be found in the Supporting Information). The sample was then rotated by a fraction of a degree and repeatedly imaged until 1313 images were collected from the sample as it was rotated through 180°. The software Xi-Cam [40] and a Python script were used to create 3D reconstructions of cells. Cells were imaged in their original pouches at 2x and 4x magnification, corresponding to pixel sizes of 3.44 and 1.72  $\mu$ m respectively. Cross-sectional slices were stacked and rendered by the software ImageJ to visualize the interior of the cells and track features of interest.

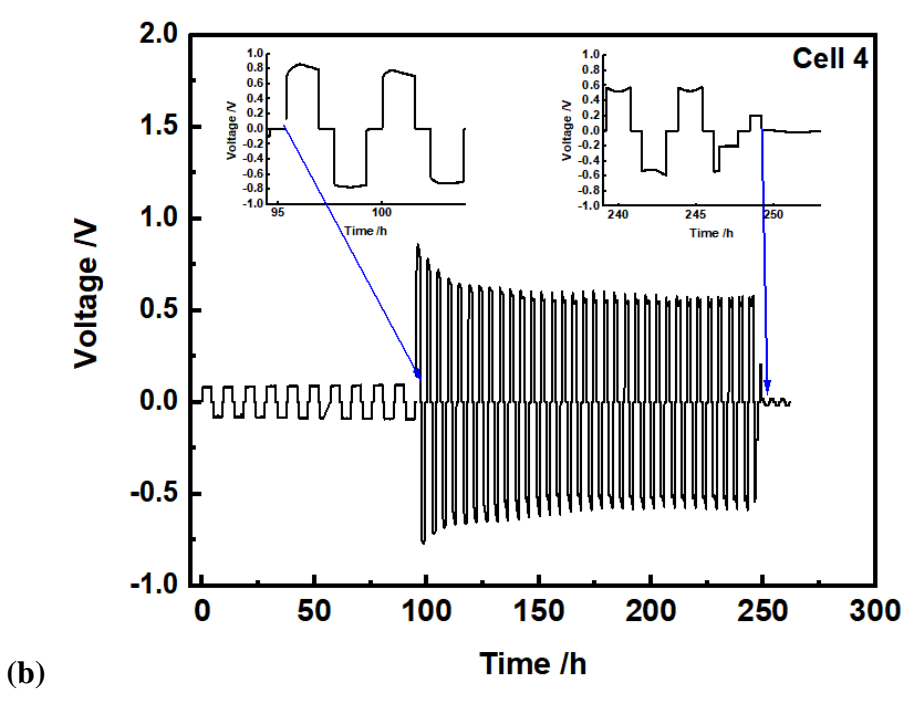
#### RESULTS AND DISCUSSION

Figure 2 (a) presents a typical overvoltage curve as a function of time for a cell cycled at i = 0.1mA cm<sup>-2</sup>. The first 10 cycles (up to 100 h) are the conditioning cycles where a galvanostatic current density of i = 0.02 mA cm<sup>-2</sup> was applied; this step provides a uniform initial state for the experiments. We posit that the conditioning cycles lead to the formation of quasi-stable electrolyte electrode interfaces. In the succeeding cycles, the cell was at the current density of i=0.1 mA cm<sup>-2</sup>. The time gaps correspond to times where the cell was paused (always after a full cycle and the rest period) in order image the cell (after 40 cycles and 87 cycles). The cell voltage is about 300 mV when +i is applied and about -300 mV when -i is applied. The first two cycles at i (inset in Figure 2(a)) show an instantaneous rise in cell voltage followed by a very slow increase. Once the current is stopped after each polarization the voltage immediately drops to zero. This squarewave-like behavior is characteristic for a single ion conductor as the passage of current does not induce a gradient in the concentration of Li<sup>+</sup> ions. Small departures from a perfect square-wave are expected because the transference number of our electrolyte is not exactly unity. The right inset presents the last two cycles of the cell. The cell voltage has the same square wave shape, and a few spikes are evident in the some of the cycles (**Figure 2** (a)). However, the cell voltage seems entirely stable until failure is seen in the last cycle of the right inset. On average, the cells run at a current density of i = 0.1 mA cm<sup>-2</sup> had a cell lifetime of  $189 \pm 68$  cycles.

**Figure 2 (b)** presents a typical cell voltage as a function of time for a cell cycled at i = 0.3 mA cm<sup>-2</sup>. After the first 10 conditioning cycles the cell voltage increases to 800 mV which is roughly a factor of three higher than the voltage obtained at 0.1 mA cm<sup>-2</sup>, as expected from Ohm's law. The voltage profiles at i = 0.3 mA cm<sup>-2</sup> are less square-wave-like compared to those at i = 0.1 mA cm<sup>-2</sup>. The voltage towards the end of each half cycle is roughly 8-9 % larger compared to the voltage in the middle of each half cycle (estimated square-wave plateau), e.g. 575 mV compared to 530 mV

for the last successful cycle of Cell 4. Polarization effects seem to be more present at this current density towards the end of the cycling, which is indicative of reaching the limits of this single-ion conducting polymer electrolyte. After about five cycles, the average overvoltage stabilizes at roughly 530 mV before cell failure is seen (right inset of **Figure 2 (b)**). On average, the cells run at a current density of i = 0.3 mA cm<sup>-2</sup> had a cell lifetime of  $28 \pm 3$  cycles.





**Figure 2**: Overvoltage profiles of two exemplary Li//Li cells cycling at 25 °C and a current density of (a) 0.1 mA cm<sup>-2</sup> (capacity of 0.4 mAh cm<sup>-2</sup>) and (b) 0.3 mA cm<sup>-2</sup> (capacity of 1.2 mAh cm<sup>-2</sup>), demonstrating interfacial stability above 240 cycles and 30 cycles, respectively. Each full cycle takes approximately 10 h, including 8 h of Li stripping and plating and 2h rest steps including impedance measurements. Conditioning cycles were performed at 0.02 mA cm<sup>-2</sup> for the first 100 h.

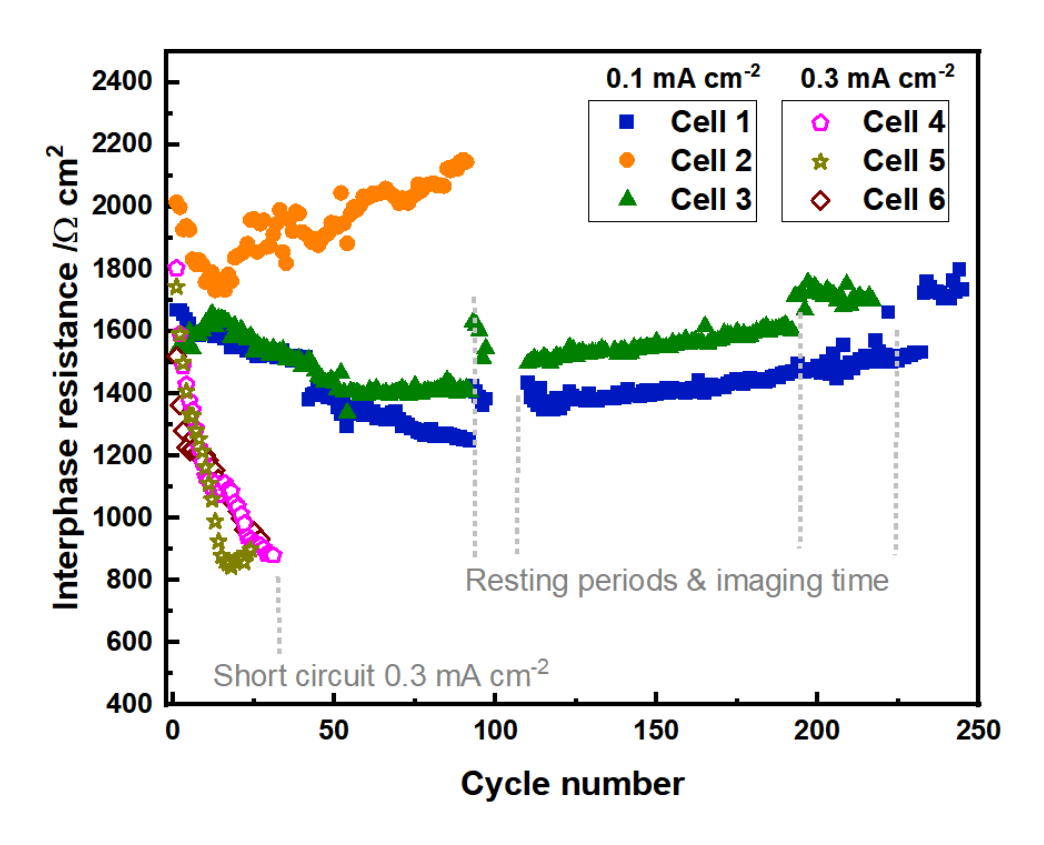


Figure 3: Comparison of the development of the interphase resistance upon cycling of Li//Li cells with current densities of 0.1 mA cm<sup>-2</sup> (Cell 1, 2, 3) and 0.3 mA cm<sup>-2</sup> (Cell 4, 5, 6), respectively. Cell 1 and Cell 3 exhibit relatively similar interphase resistances, whereas for Cell 2, a rapid increase leads to a reduced cycle life. Sudden changes in interphase resistance are a result of prolonged resting time used for X-Ray tomography experiments. The interphase resistance of the three cells cycled at 0.3 mA cm<sup>-2</sup> is relatively similar with a rapid decrease until short circuit after around 30 cycles. The interphase resistance is normalized to the electrode area by multiplying with the area of one electrode and dividing by two (accounting for the symmetrical cell). Between cycle 97 and 110, there was no impedance data recorded due to a software issue. The sudden increase in interfacial resistance after the resting periods originates from continuous interfacial reactions during rest.

**Figure 3** shows the time-dependence of interphase resistance,  $R_i$ , of the cycled cells. Since the solid electrolyte interphase (SEI) has a finite width,  $R_i$  contains contributions from both two-dimensional interfaces and three-dimensional interphases. The interphase resistance was obtained from the electrochemical impedance spectra by subtracting the bulk resistance from the total resistance. Identification of bulk and interphase resistance is done using a distribution of relaxation times and

taking the high frequency resistance as bulk resistance (further details are summarized in the Supporting Information). The general characteristics of Cells 1-3 cycled at i = 0.1 mA cm<sup>-2</sup> are qualitatively similar – an early decline in  $R_i$  followed by an increase. The interphase resistances of Cell 1 and Cell 3 follow the same trend upon cycling: during the first 100 cycles, the resistance decreases from about 1600  $\Omega$  cm<sup>2</sup> to roughly 1200 and 1400  $\Omega$  cm<sup>2</sup> for Cell 1 and Cell 3, respectively, before it gradually increases until the end of cycle life (> 220 cycles). We posit that the decrease in the area-specific resistance is due to both roughening of the electrode-electrolyte interfaces and associated enhanced interfacial reactions. The processes of Li activation/SEI stabilization and surface roughening can be considered closely related, as increasing microscopic surface area also facilitates interfacial reactions and associated formation of interphases. Cell 2 is an outlier, the decline in resistance from 2000 to 1700  $\Omega$  cm<sup>2</sup> occurs during the first 15 cycles, before the cell resistance increases, ultimately leading to failure after 91 cycles. One possible explanation of this behavior could be that the solvent content of this sample was lower than expected, which would result in higher interfacial resistance. Upon cycling, interfacial reactions consume parts of the solvent, which may eventually impair the overall cell performance and facilitate faster decay (increase in resistance). The general characteristics of Cells 4-6 cycled at i = $0.3 \text{ mA cm}^{-2}$  are qualitatively different from cells cycled at  $i = 0.1 \text{ mA cm}^{-2}$  (**Figure 3**). In these cells, we see a precipitous drop in  $R_i$  from 1600 to 900  $\Omega$  cm<sup>2</sup> in the first 25 cycles leading to cell failure.

DRT analysis of the time-dependent impedance data led to further insights to underpin the observations. The impedance data of Cell 1 is presented as Nyquist plots (**Figure 4 (a)**) while the DRT analysis results are shown as  $h_k$  versus  $\log(\tau_k)$  plots (**Figure 4 (b)**).  $h_k$  is the resistive contribution at a given time constant  $\tau_k$ . The area under the DRT curve is proportional to  $R_i$  and

represents the sum of resistive contributions characterized by different time constants. The reduction in the area in Cell 1 between cycles 1 and 40 is consistent with decline in  $R_i$  noted above. The timescale associated with the ion transport (including charge transfer) can be determined from the location of the peak position,  $\tau_{\text{peak}}$ , which is at about 6 ms, which provides insight into the origin of the decline in  $R_i$ . The measured timescale must reflect the time required for charge transport across from the bulk, through the SEI, and into the electrode. We conclude that there is no significant change in the nature of the SEI during the first 40 cycles – there is, however, an increase in interfacial area due to, perhaps, nonplanar lithium deposition and concomitant roughening of the interface. This decrease in  $R_i$  and fixed  $\tau_{\text{peak}}$  continues until cycle 90. If we assume that  $R_i$  decreases mostly due to increased roughness, we conclude that the additional interfacial area at cycle 90 relative to the pristine cell is between 15 and 20% for Cells 1-3 (see SI for data from Cells 2 and 3). The increase in  $R_i$  at later cycles is associated with the detection of a slower transport process; see cycle 245 data in **Figure 4** (b). This implies that transport through the interfaces and interphases becomes slower as cell failure is approached. Note that the underpinnings of this observation are unclear yet, but it may reflect a thicker SEI. The impedance data of Cell 4 is presented as Nyquist plots (**Figure 4** (c)) while the DRT analysis results are shown as  $h_k$  versus  $\log(\tau_k)$  plots (**Figure 4** (d)). Here we observe a monotonic decline in  $R_i$  with a slight change in  $\tau_{peak}$  from about 6 ms to 4 ms throughout the experiment. This slight decrease in time constant could be indicative of enhanced interfacial processes and associated changes in the nature of the SEI. Simultaneously, as can be seen in **Figure 3**, for cells cycled at the higher current density, the interfacial resistance decreases substantially faster compared to cells cycled at lower current density. This is likely due to the larger amount of Li cycled and accumulated, which then leads to both higher surface area and slightly

enhanced interfacial reactions. We find that the additional interfacial area at failure relative to the pristine cell is about 40% for Cells 4-6 (see SI for data from Cells 5 and 6).

It is clear from **Figure 3** and **Figure 4** that there is a qualitative difference in the response of the considered gel electrolyte when it is cycled at 0.1 and 0.3 mA cm<sup>-2</sup>. In particular, increasing current density by a factor of 3 doubles the surface roughness; also, the slow increase in  $R_i$  is not seen at 0.3 mA cm<sup>-2</sup>. Further insight into these differences is obtained by X-ray microtomography.

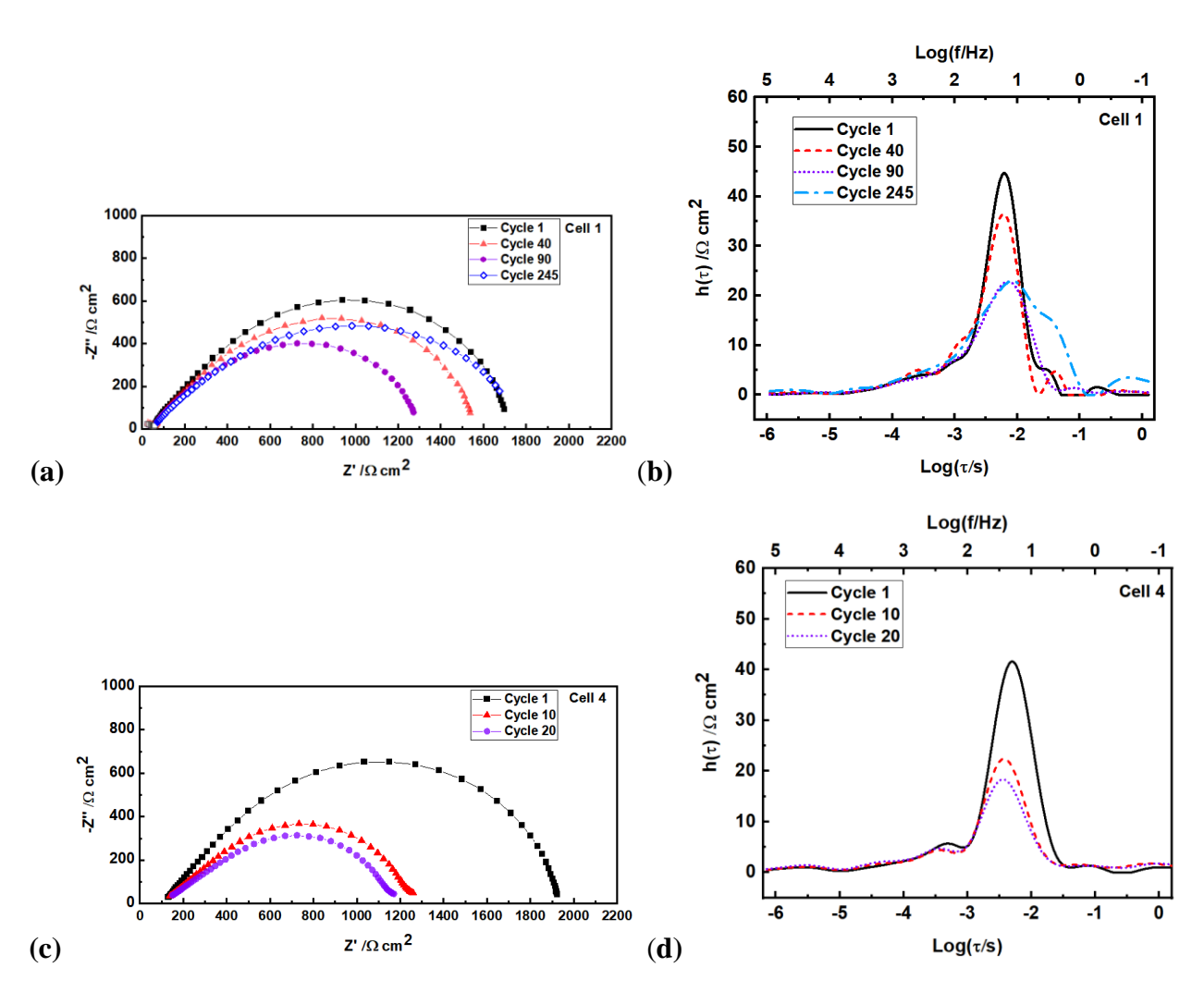


**Figure 4**. (a): Nyquist plots of Cell 1 after one, 40 and 90, and 245 cycles at a current density of  $i = 0.1 \text{ mA cm}^{-2}$ . The impedance spectra were measured after 45 min of equilibration at Open Circuit Voltage (OCV) after each cycle. (b): DRT analysis of Cell 1 at cycle one, 40, 90 and 245. (c) Nyquist plots of Cell 4 after one, 10 and 20 cycles at a current density of  $i = 0.3 \text{ mA cm}^{-2}$ . (d) DRT analysis of Cell 4 at cycle one, 10, and 20. The main contribution to the internal resistance is related to

migration through interphases (SEI) and charge transfer at the electrolyte/electrode interfaces and becomes more heterogeneous over cycling. The increase in interphase resistance can be seen in the increasing peak width and associated increase in peak area (which corresponds to the interphase resistance).

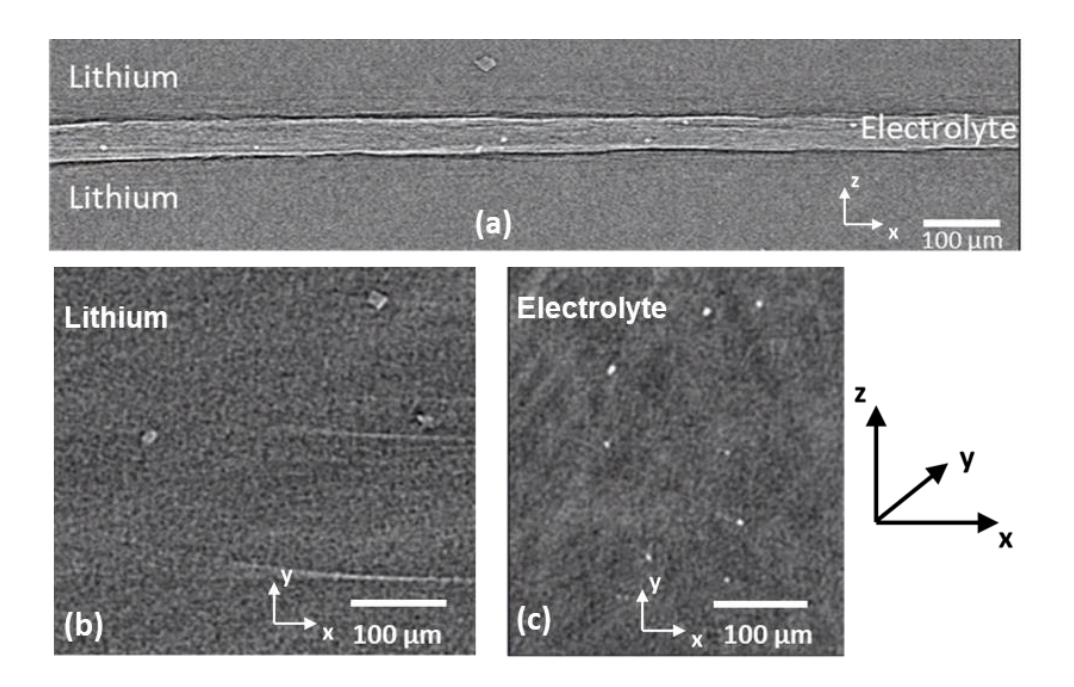


Figure 5. Reconstructed X-ray tomograms of an exemplary symmetric Li||Li cell. (a) Cross-sectional slice after the passage of current for conditioning cycles at i = 0.02 mA cm<sup>-2</sup>. The polymer electrolyte membrane appears as a light and unbroken band separating the two Li metal electrodes. No Li protrusions were observed in any symmetric cells after conditioning cycles. Bright specks are visible inside the electrolyte, and a faceted Li impurity is visible in the top Li electrode. (b) and (c): Top views of tomogram slices through (b) the volume of the Li showing crystalline impurities and (c) through the volume of the electrolyte showing impurities contained inside the electrolyte and that are randomly distributed. Grey pixel values of both impurities are different, the one contained inside the polymer are much brighter signifying a higher electron dense nature than the impurity contained inside the Li metal. Moreover, the impurities inside the electrolyte are round-shaped, while the Li impurities are faceted.

Hard X-ray microtomography was performed for cells after conditioning cycles (before cycling at  $i = 0.1 \text{ mA cm}^{-2}$  and  $i = 0.3 \text{ mA cm}^{-2}$ ), as well as after 40 cycles, 87 cycles (for cells cycled at i = 0.3 mA), as well as after 40 cycles, 87 cycles (for cells cycled at i = 0.3 mA).

0.1 mA cm<sup>-2</sup>) and after failure. **Figure 5 (a)** presents a typical example of a cross-sectional slice through the reconstructed X-ray tomogram of a symmetric Li||Li cell after 10 conditioning cycles at i = 0.02 mA cm<sup>-2</sup> (corresponding to ca. 0.4 µm of Li plated and stripped per cycle). Three distinct regions are visible in the tomogram - two dark gray bands on the top and bottom represent the Li metal electrodes, while a bright middle band reflect the polymer electrolyte. The grayscale of each pixel is proportional to the local X-ray absorption coefficient; a brighter pixel corresponds to a material with a higher absorption coefficient. Li metal appears dark as it is has the lowest X-ray absorption coefficient [41]. The polymer electrolyte appears brighter due the presence of atoms that are heavier than lithium. Imaging samples containing interfaces results in the Fresnel phase contrast that shows as thin dark and bright bands at the interface. This is evident at the electrolytelelectrode interfaces in Figure 5 (a) [42,43]. Note that Fresnel phase contrast affects all interfaces including new interfaces formed due to non-planar electrodeposition of Li metal. After conditioning cycling, the cells do show no notable features, implying that during this step the electrodeposited Li results in planar deposition [27]. It is important to notice a bright diamond shaped object inside the top Li electrode in Figure 5 (a), which is a Li impurity contained in the Li metal foil. In addition, bright round shaped specks indicate impurities trapped in the gel electrolyte. It is possible that these are impurities left over from fabrication of the membrane, such as agglomerated PVDF-HFP or undissolved single-ion conducting polymer. During membrane fabrication, these components were added into solvent (NMP) and stirred overnight at 60 °C. It is possible that the mixing time was too short and individual agglomerations remained undissolved. Upon inspection of the entire imaged cells, numerous impurities are visible in both the Li metal electrodes and the electrolyte. Figure 5 (b) and (c) show top view slices through (b) the volume of the Li metal electrode and (c) the volume of the polymer electrolyte. Crystalline impurities inside Li metal electrodes have been previously

reported in the literature, [26,29,41] and are faceted impurity particles that comprise either lithium oxide (Li<sub>2</sub>O), lithium hydroxide (LiOH) or lithium nitride (Li<sub>3</sub>N) [26]; they vary in size and shape [7]. **Figure 5** (c) presents bright approximately spherical impurities randomly distributed inside the volume of the polymer electrolyte. They appear to have a variety of sizes from about 3 to 50 µm in diameter (see Figure S9 in SI for further examples). The cycled cells at both i = 0.1 and 0.3 mA cm<sup>-</sup> <sup>2</sup> presented three distinct nonplanar morphologies which are shown in **Figure 6** where we show cross sectional slices through the reconstructed X-ray tomograms. Figure 6 (a) presents an example of a typical singular globular protrusion, surrounded by an electrolyte "sac", which appears as a thin bright line inside the Li electrode. Note that the grayscale of the globule is similar to that of the Li foil suggesting that the globule is a dense Li deposit. At the top of the globular protrusion, a bright round shaped impurity can be seen suggesting that it was the cause of the nucleation of the globule. This impurity, which we surmise was located in the electrolyte (perhaps at the electrodeelectrolyte interface), is pushed into the electrode by repeated cycling. The lower panel in **Figure** 6 (a) shows a simplified drawing of a globular defect. In previous studies of cycling block copolymer electrolytes containing an added salt, cycling led to the formation of multi-globular deposits [6,7,25,28]. The qualitative difference in globule structure in polymer electrolytes with a mobile cation (present study) and polymer electrolytes with a mobile cations and anions is noteworthy, though a mechanistic understanding of this difference requires further study.

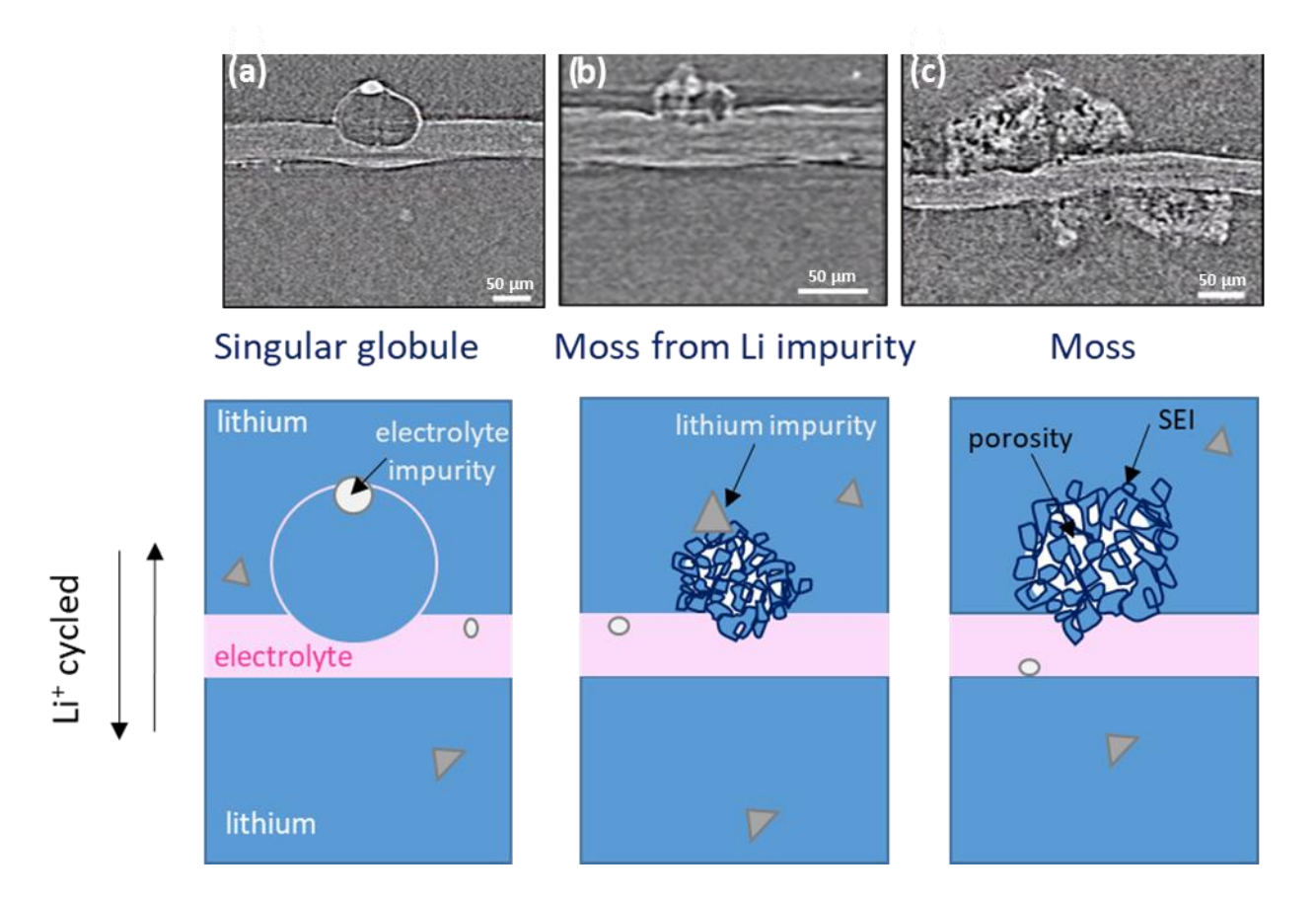
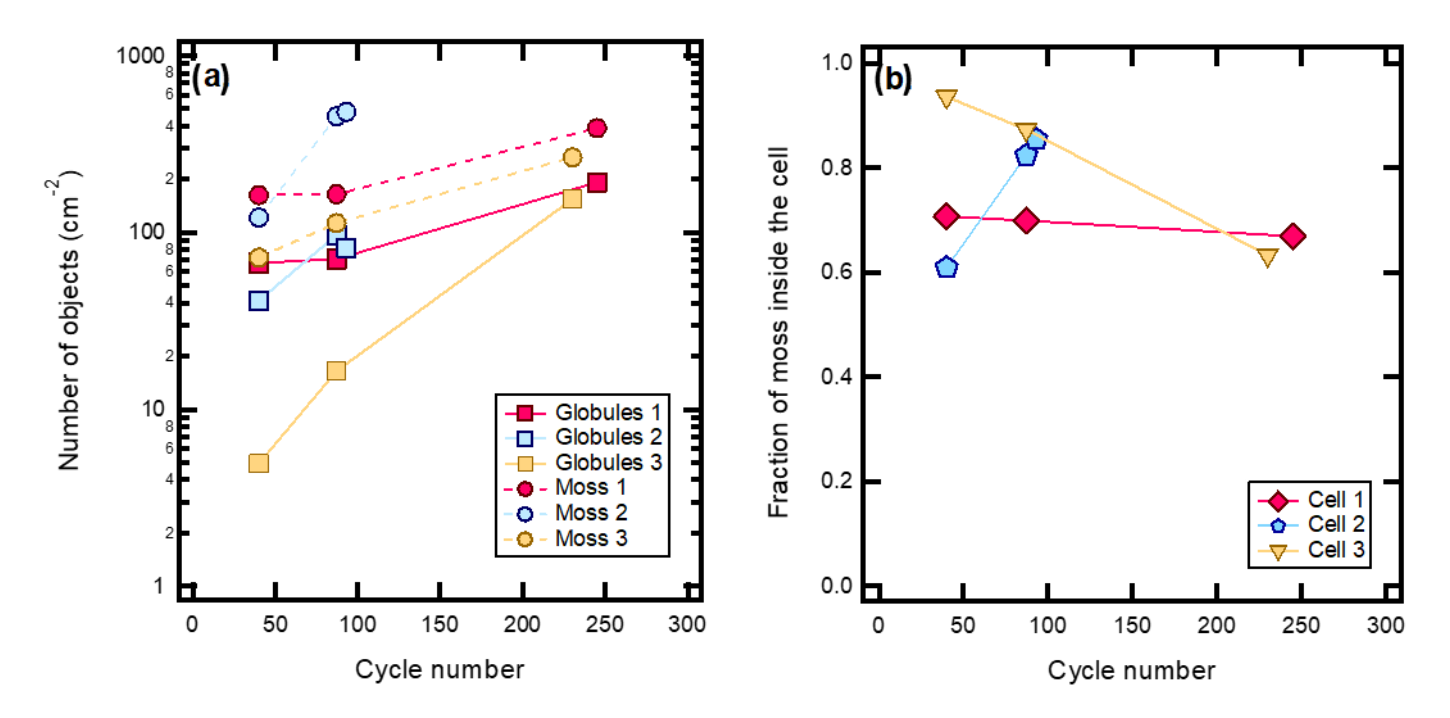


Figure 6. Cross-sectional slices through the reconstructed X-ray tomograms representing different types of non-planar Li electrodeposition found in all cells cycled at i=0.1 and 0.3 mA cm<sup>-2</sup> (a) Li globule nucleated from an electrolyte impurity, the grey pixel value of the electrodeposited Li is similar to the Li electrode pixel value. (b) Mossy Li electrodeposits nucleated from a Li impurity, gray pixel values are somewhat brighter than the Li electrode gray pixel value suggesting a change of Li nature (SEI formation and side reaction), moreover, the presence of dark spots indicate that these electrodeposits are porous. (c) Mossy Li electrodeposits not nucleated from a Li impurity particle. Non-planar deposition appears in both top and bottom electrodes. Below each type of non-planar electrodeposition, a scheme was given for a better comprehension.

**Figure 6 (b)** shows an example of a mossy structure that was nucleated from a Li impurity, while **Figure 6 (c)** displays an example of mossy structure without any impurity. Both structures are very similar. The gray pixel values are somewhat brighter than the Li electrode gray pixel value suggesting salt has been incorporated into these structures. In addition, the presence of dark spots

indicates that these electrodeposits are porous. These objects are bush-like and vary in length from a few  $\mu m$  to hundreds of  $\mu m$  (**Figure 6 (c)**). The resolution of the microtomography (1 pixel = 1.72  $\mu m$ ) is not sufficient to resolve the details of these objects, which in the literature have been seen as small as 0.1  $\mu m$  [6]. Similar mossy deposits were observed in previous studies of cycling block copolymer electrolytes containing an added salt at similar current densities [27].



**Figure 7**. (a) Evolution of the number of globular protrusions and mossy Li as a function of the number of cycles for the three symmetric Li cells at a current density of 0.1 mA cm $^{-2}$ . (b) Fraction of mossy structures inside the cell using Equation 1 for the three cells cycled at a current density of 0.1 mA cm $^{-2}$  as a function of cycle number.

Globular protrusions and mossy Li deposits were manually counted for each cell at each time step (for the cells cycled at i = 0.1 mA cm<sup>-2</sup>). The electrode-electrolyte interface examined in this analysis was 60.8 mm<sup>2</sup>. **Figure 7** (a) shows the total numbers of the two types of deposits in Cells 1, 2, and 3; cycling leads to an increase in both types of deposits. The cells contain more mossy deposits than globules and, upon cycling, the number of deposits increases two- to ten-fold.

Cell 2, the outlier as identified above, had the largest number of mossy deposits, increasing from 100 to 500 until cell failure, it also exhibited the shortest cycle life.

The data in **Figure 7** (a) enables calculation of the fraction of mossy deposits in our cells:

Fraction of moss = 
$$\frac{\text{Number of mossy deposits}}{\text{Number of mossy deposits} + \text{Number of globules}}$$
 (1)

This fraction ranges between 0.60 and 0.95, indicating that mossy deposits are the dominant type of protrusion in the cycled cells, even at i = 0.1 mA cm<sup>-2</sup>. We show below that only mossy deposits are evident at the higher current density. In the three cells examined at i = 0.1 mA cm<sup>-2</sup>, the moss fraction decreases slightly with cycle number in Cell 1, increases in Cell 2, and decreases in Cell 3. It is evident that cell failure at i = 0.1 mA cm<sup>-2</sup> is dependent on the presence of both globular and mossy deposits, which finally results in a short circuit and can vary from cell to cell. As the number of investigated cells is limited in this study, we do not consider our findings as quantitatively representative results, but rather as qualitative examples for processes and failure modes that may occur in cells during electrochemical operation. The relatively large deviations between each cell in **Figure 7** furthermore demonstrate the complexity of systems involving lithium metal and their sensitivity to perhaps yet unknown variables (such as e.g. microscopic impurities).

Non-planar deposits in Cells 1-3 were not uniformly distributed through the cell. While large regions of the electrolyte remain intact and participate to planar deposition, particular "hot-spots" showed nonplanar electrodeposition objects, including mossy and globular deposits (Figure S11, Supporting Information). The globular protrusions observed at cells cycled at 0.1 mA cm<sup>-2</sup> are much larger compared to the theoretical amount of Li plated per half cycle (~2 µm of or 0.1 mg cm<sup>-2</sup>), which indicates large accumulation of Li deposits over cycling. The local factors that cause the

nucleation and growth of nonplanar deposits are complex; evidence suggests that the presence of a defect in one location promotes the nucleation and growth of more defects in its vicinity. Local current densities at impurities and roughened surfaces are expected to be substantially larger compared to the averaged macroscopic current density and thus facilitate local charge accumulation and reactions. As the globular protrusions are growing with cycling number, it can be deduced that Li deposition at globular sites is favored, whereas Li dissolution is less favored (or less efficient) at globular sites (leading to a net growth of Li deposits). Furthermore, the Li reservoirs on both electrodes can be considered infinite and thus can contribute to the local accumulation of Li deposits. It is unclear if such accumulation of large globular deposits can be minimized by high precision membrane fabrication and cell building processes. The blended polymer electrolyte may also impact inhomogeneous Li deposition, as phase separation is present in this class of materials. In a recent study on the same polymer electrolyte and derivatives thereof, it was found that the formation of domains of poorly conducting crystalline PVDF-HFP and well conducting intermixed domains (supported by structural solvent) lead to preferential Li conduction pathways and eventually impact Li deposition [14].

**Figure 8** depicts different stages of growth of a nonplanar defect: (a) a globular defect nucleated from impurities in the electrolyte, (b) a mossy defect without a visible impurity, and (c) a mossy defect nucleated at an impurity in the electrode. We define a Cartesian coordinate system with the z-axis oriented in the nominal direction of the applied current (see **Figure 8**). Tomography images of the same defect at different stages of cycling (Cycle 40 and Cycle 87) allow quantification of the growth rate of each protrusion. In **Figure 8** (a) we see two sets of electrolyte impurities that appear to have nucleated on two connected globules. Focusing on the larger globule, we find that it increases by roughly 20  $\mu$ m in all 3 (x, y, z) between Cycle 40 and 87, which implies additional

lithium ions (in excess of those transported due to the applied current density) are transported through the electrolyte "sac" and they get incorporated in the globule. In **Figure 8 (b)** we see a mossy defect with no visible sigh of a nucleating defect that doubles in size in all directions. A large fraction of the defect lies within the electrode. In **Figure 8 (c)** we see the growth of a mossy defect nucleated at an electrode impurity. This defect does not grow appreciably during cycling.

In the current approach, we identify the same defect manually by scanning the tomograms. To obtain statistical information about the growth of defects we will need to automate the process. This is not trivial as the contrast obtained in each cell varies due to slight changes in sample and instrument configuration. This is unavoidable because successive tomograms are obtained during beam-time experiments separated by several months.

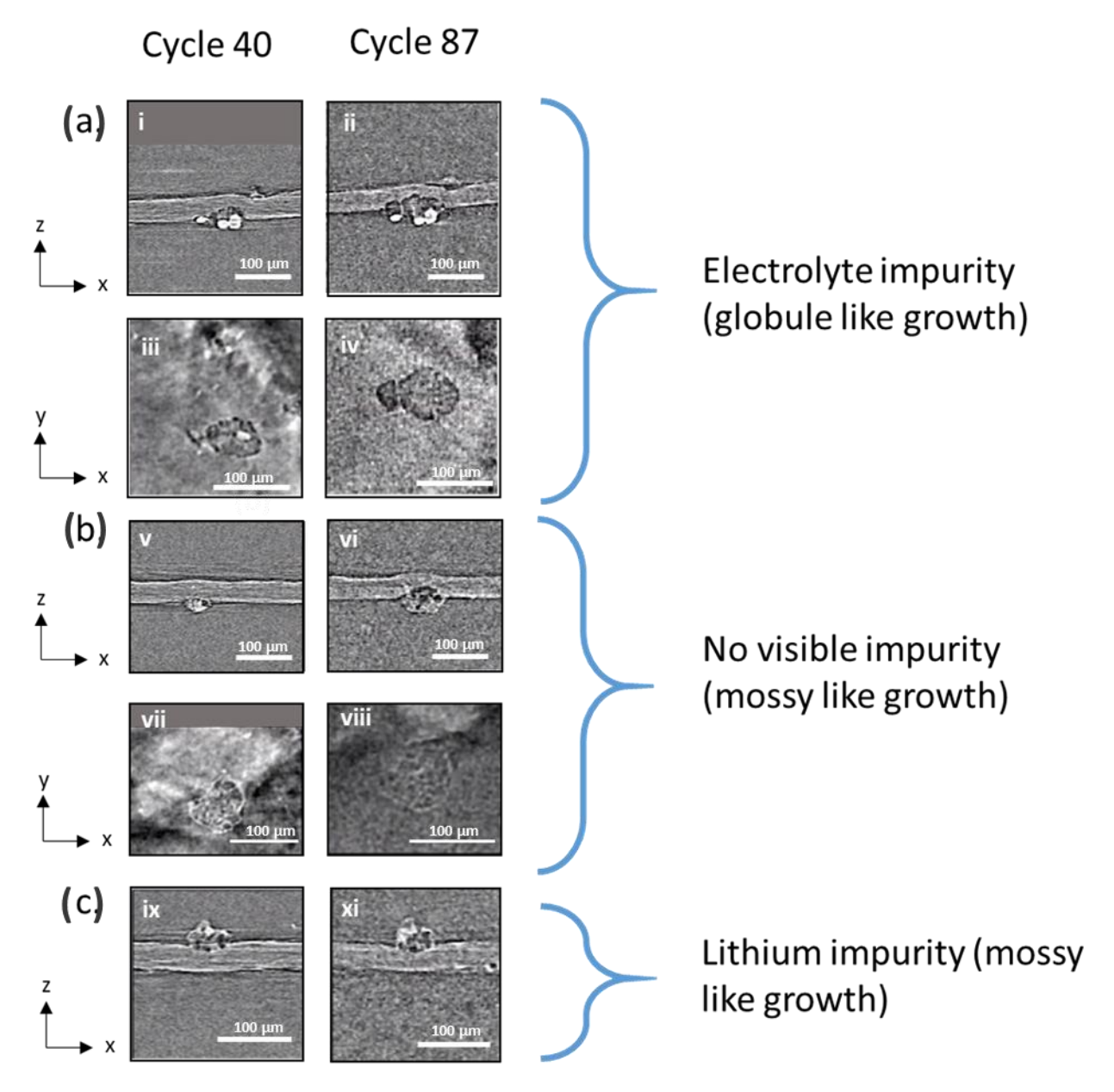


Figure 8. Time-stop imaging of a non-planar Li electrodeposition inside a symmetric Li//Li cell over the course of a galvanostatic cycling experiment. Left to right tracking of typical dynamics of a single globule as time increases. (a) Li globule nucleated from an impurity located inside the electrolyte, (b) mossy Li electrodeposit without visible impurity and (c) mossy Li electrodeposit nucleated from an impurity located inside the Li electrode. (i–ii; v-vi; ix-xi) Orthogonal cross-sections through non-planar Li electrodeposits in the xz-plane, (i, v and ix) after 40 cycles at 0.1mA cm<sup>-2</sup> and (ii, vi and xi) after 87 cycles at 0.1 mA cm<sup>-2</sup>. (iv-vi; vii-viii) Top view slices in the xy-plane of the bottom electrolyte/Li interface at the non-planar electrodeposit location; columns of images correspond to the same object at identical time, varying only in orientation.

**Figure 9 (a)** and **(b)** presents two tomograms of the same globular structure found in Cell 1 after failure, this globular structure is responsible for the cell short circuit after cycling at 0.1 mA cm<sup>-2</sup>. **Figure 9 (a)** displays the electrolyte impurity nucleating the globular structure (top lithium electrode), while **Figure 9 (b)** shows how the globule is spanning the electrolyte (bottom lithium electrode) and short the cell. It is important to notice also that this structure is located within a mossy lithium deposit. However, the failure of the cell is attributed to the globular structure. All of the tomograms of electrolyte-spanning defects had a similar character. This suggests that globular defects nucleated from electrolyte impurities provide the dominant failure mode at i = 0.1 mA cm<sup>-2</sup>. This is somewhat surprising, as the majority of the defects are not globular.

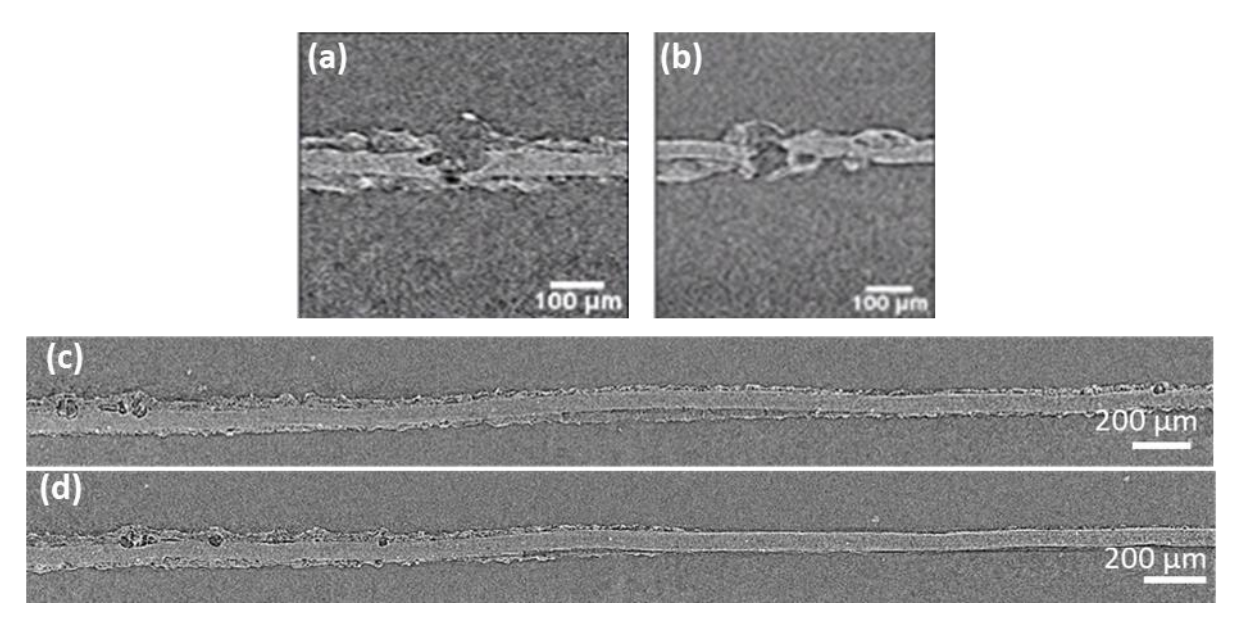


Figure 9. (a), (b): Cross section tomogram of the globular protrusion causing the short circuit in Cell 1 cycled at  $0.1 \text{ mA cm}^{-2}$ . (a) electrolyte impurity nucleating the globular protrusion and (b) the same globular structure at a different angle showing the actual short circuit. The Li grey value spans across the electrolyte membrane. All short circuits in the cells imaged originate from a globular protrusion nucleated from an electrolyte impurity. (c), (d): Tomograms of examples of non-planar Li electrodeposition for cells cycled at  $i = 0.3 \text{ mA cm}^{-2}$  after failure. Mossy Li is formed in a continuous way on both top and bottom electrodes. Singular globules are also seen, some nucleated at electrolyte impurities. Some parts of the cell present neither mossy Li nor globular protrusion.

Tomograms of cells cycled at i = 0.3 mA cm<sup>-2</sup> are strikingly different, as documented in **Figure 9** (c) and (d). Cells 4, 5, and 6 failed before the first planned tomography experiment (after 40 cycles). We thus only have images of failed cells; two examples are shown in **Figure 9** (c) and (d). At this high current density, significant fractions of the electrode-electrolyte interface are covered with mossy defects with a few isolated globules (see **Figure 9** (c)). The defect density was non-uniform as shown in **Figure 9** (d) – regions with a high density of defects were right next to pristine-looking regions with no defects. We were not able to detect electrolyte-spanning shorts in any of these cells, indicating that the shorts were either in regions that could not be resolved (*e.g.*, edges of the cell) or the shorts were thin filamentous structures (perhaps dendritic in nature) with length scales below the resolution limit of our instrument. Although there are, generally speaking, many different processes eventually causing cell failure in lithium based systems[44,45], the main failure process at a higher current density is, in our case, likely based on kinetic limits of the electrolyte in combination with substantial interfacial reactions due to large amounts of high surface area Li (here mossy-type).

#### **CONCLUSION**

Symmetric Li||Li cells with a single-ion conducting polymer electrolyte gel membrane based on a polysulfonamide backbone were cycled at 25 °C with current densities, *i*, of 0.1 mA cm<sup>-2</sup> and 0.3 mA cm<sup>-2</sup>. At 0.1 mA cm<sup>-2</sup> cells lasted for an average of 190 cycles. In contrast, cells cycled at 0.3 mA cm<sup>-2</sup> lasted for an average of only 30 cycles. Since the amount of lithium cycled was a factor of three higher at the higher current density, the total number of Coulombs passed before failure at 0.1 mA cm<sup>-2</sup> is about a factor of two larger than that at 0.3 mA cm<sup>-2</sup>. Electrochemical impedance spectroscopy after each Li plating/stripping cycle was utilized to monitor the evolution of interfacial resistances upon cycling. Cells cycled at 0.1 mA cm<sup>-2</sup> initially showed a decrease in

area-specific interfacial resistance,  $R_i$ , followed by a steady increase until short circuit, whereas cells cycled at 0.3 mA cm<sup>-2</sup> only showed a decrease in  $R_i$  until cell failure. DRT analysis of the impedance spectra revealed roughening of the electrode electrolyte interface as the cause of the decrease in  $R_i$  at both current densities. Hard X-Ray microtomography confirmed this conclusion and provided microscopic details that are difficult to glean from impedance alone. Cycling resulted in the formation of either mossy or individual globular defects. Many of the defects appear to be nucleated by impurities in either the electrolyte membrane or the electrode. Individual defects formed at 0.1 mA cm<sup>-2</sup> were identified manually and some aspects were quantified. The average defect density at failure was about 100 cm<sup>-2</sup>. The defects were localized in certain regions of the cell – other regions of the cycled cells remained unchanged in spite of cycling. At 0.3 mA cm<sup>-2</sup>, mossy defects formed a contiguous "layer" between the electrode and the electrolyte. The depths within the electrodes at which defects were found were often as high as 50 µm, and these depths are much larger than the thickness of the cycled lithium layers (3 and 6 µm per cycle at 0.1 and 0.3 mA cm<sup>-2</sup>). Cell shorts wherein lithium metal connected the two electrodes were only directly observed in failed cells cycled at 0.1 mA cm<sup>-2</sup>. They were single globules located within or near mossy defects. The X-ray tomography experiments provided proof for our hypothesis that the initial decrease in  $R_i$  during cycling was mostly due to roughening of the electrode electrolyte interface. Even at i = 0.3 mA cm<sup>-2</sup>, the decrease in  $R_i$  just prior to failure is modest – 40%, indicating an increase in interfacial area of 40 %. One may expect a larger increase based on the assumed character of mossy deposits. The non-uniformity of the roughening makes direct connection between the X-ray tomography and impedance experiments challenging. Our study provides insights into the nature of failure when a single-ion conducting polymer gel electrolyte is utilized to cycle lithium metal electrodes. Developing approaches to prevent these failure modes seem warranted, including better engineering of the electrode-electrolyte interface, the SEI, and the production of electrolytes and lithium metal electrodes that are free of impurities.

# **SYMBOLS and ABBREVIATIONS**

Li	Lithium
PSA	Polysulfonamide
EC	Ethylene carbonate
PC	Propylene carbonate
PVDF-HFP	Poly(vinylidene fluoride-co-hexafluoropropylene
NMP	N-Methyl-2-pyrrolidone
EIS	Electrochemical impedance spectroscopy
DRT	Distribution of relaxation times
SEI	Solid electrolyte interphase
λ	Optimization parameter for DRT
τ	Time constant (inverse angular frequency)
R	Resistance
С	Capacitance

# **SUPPORTING INFORMATION**

Overvoltage profiles of further cells, Impedance and DRT spectra of further cells, Details on DRT analysis and algorithm, Further X-Ray microtomographic images

#### ACKNOWLEDGMENTS

This work was funded by the US-German collaboration on "Interfaces and Interphases in Rechargeable Li-metal based Batteries", supported by the joint research project "LISI" by the German Federal Ministry of Education and Research (BMBF: 13XP0224A) and the US Department of Energy (DOE) (DE-AC02-05CH11231) to LBNL.

#### REFERENCES

- [1] Cheng, X.-B.; Zhang, R.; Zhao, C.-Z.; Zhang, Q. Toward Safe Lithium Metal Anode in Rechargeable Batteries: A Review, Chemical Reviews 2017, 117 (15), 10403
- [2] Wu, H.; Jia, H.; Wang, C.; Zhang, J. G.; Xu, W. Recent Progress in Understanding Solid Electrolyte Interphase on Lithium Metal Anodes, Advanced Energy Materials 2020, 11 (5), 2003092
- [3] Heubner, C.; Maletti, S.; Auer, H.; Hüttl, J.; Voigt, K.; Lohrberg, O.; Nikolowski, K.; Partsch, M.; Michaelis, A. From Lithium-Metal toward Anode-Free Solid-State Batteries: Current Developments, Issues, and Challenges, Advanced Functional Materials 2021, 31 (51), 2106608
- [4] Winter, M.; Barnett, B.; Xu, K. Before Li Ion Batteries, Chemical Reviews 2018, 118 (23), 11433
- [5] Ryou, M.-H.; Lee, Y. M.; Lee, Y.; Winter, M.; Bieker, P. Mechanical Surface Modification of Lithium Metal: Towards Improved Li Metal Anode Performance by Directed Li Plating, Advanced Functional Materials 2015, 25 (6), 834
- [6] Frenck, L.; Sethi, G. K.; Maslyn, J. A.; Balsara, N. P. Factors That Control the Formation of Dendrites and Other Morphologies on Lithium Metal Anodes, Frontiers in Energy Research 2019, 7, 115
- [7] Frenck, L.; Maslyn, J. A.; Loo, W. S.; Parkinson, D. Y.; Balsara, N. P. Impact of Salt Concentration on Nonuniform Lithium Electrodeposition through Rigid Block Copolymer Electrolytes, ACS Applied Materials & Interfaces 2019, 11 (51), 47878
- [8] Li, J.; Cai, Y.; Wu, H.; Yu, Z.; Yan, X.; Zhang, Q.; Gao, T. Z.; Liu, K.; Jia, X.; Bao, Z. Polymers in Lithiumlon and Lithium Metal Batteries, Advanced Energy Materials 2021, 11 (15), 2003239
- [9] Tang, S.; Guo, W.; Fu, Y. Advances in Composite Polymer Electrolytes for Lithium Batteries and Beyond, Advanced Energy Materials 2021, 11 (2), 2000802
- [10] Nair, J. R.; Imholt, L.; Brunklaus, G.; Winter, M. Lithium Metal Polymer Electrolyte Batteries: Opportunities and Challenges, The Electrochemical Society Interface 2019, 28 (2), 55
- [11] Singh, M.; Odusanya, O.; Wilmes, G. M.; Eitouni, H. B.; Gomez, E. D.; Patel, A. J.; Chen, V. L.; Park, M. J.; Fragouli, P.; Iatrou, H.et al. Effect of Molecular Weight on the Mechanical and Electrical Properties of Block Copolymer Electrolytes, Macromolecules 2007, 40 (13), 4578
- [12] Borzutzki, K.; Thienenkamp, J.; Diehl, M.; Winter, M.; Brunklaus, G. Fluorinated Polysulfonamide Based Single Ion Conducting Room Temperature Applicable Gel-type Polymer Electrolytes for Lithium Ion Batteries, Journal of Materials Chemistry A 2019, 7 (1), 188
- [13] Borzutzki, K.; Dong, D.; Wolke, C.; Kruteva, M.; Stellhorn, A.; Winter, M.; Bedrov, D.; Brunklaus, G. Small Groups, Big Impact: Eliminating Li(+) Traps in Single-Ion Conducting Polymer Electrolytes, iScience 2020, 23 (8), 101417
- [14] Borzutzki, K.; Dong, K.; Nair, J. R.; Wolff, B.; Hausen, F.; Eichel, R.-A.; Winter, M.; Manke, I.; Brunklaus, G. Lithium Deposition in Single-ion Conducting Polymer Electrolytes, Cell Reports Physical Science 2021, 2 (7), 100496
- [15] Chazalviel, J. N. Electrochemical Aspects of the Generation of Ramified Metallic Electrodeposits, Physical Review A 1990, 42 (12), 7355

- [16] Zhu, J.; Zhang, Z.; Zhao, S.; Westover, A. S.; Belharouak, I.; Cao, P.-F. Single-Ion Conducting Polymer Electrolytes for Solid-State Lithium–Metal Batteries: Design, Performance, and Challenges, Advanced Energy Materials 2021, 11 (14), 2003836
- [17] Yang, S.; Min, X.; Fan, H.; Xiao, J.; Liu, Y.; Mi, R.; Wu, X.; Huang, Z.; Xi, K.; Fang, M. In situ Characterization of Lithium-metal Anodes, Journal of Materials Chemistry A 2022, 10 (35), 17917
- [18] Sun, M.; Liu, T.; Yuan, Y.; Ling, M.; Xu, N.; Liu, Y.; Yan, L.; Li, H.; Liu, C.; Lu, Y.et al. Visualizing Lithium Dendrite Formation within Solid-State Electrolytes, ACS Energy Letters 2021, 6 (2), 451
- [19] Hogrefe, C.; Waldmann, T.; Molinero, M. B.; Wildner, L.; Axmann, P.; Wohlfahrt-Mehrens, M. Cross-Sectional In Situ Optical Microscopy with Simultaneous Electrochemical Measurements for Lithium-Ion Full Cells, Journal of The Electrochemical Society 2022, 169 (5), 050519
- [20] Simon, F. J.; Hanauer, M.; Richter, F. H.; Janek, J. Interphase Formation of PEO20:LiTFSI–Li6PS5CI Composite Electrolytes with Lithium Metal, ACS Applied Materials & Interfaces 2020, 12 (10), 11713
- [21] Otto, S.-K.; Riegger, L. M.; Fuchs, T.; Kayser, S.; Schweitzer, P.; Burkhardt, S.; Henss, A.; Janek, J. In Situ Investigation of Lithium Metal–Solid Electrolyte Anode Interfaces with ToF-SIMS, Advanced Materials Interfaces 2022, 9 (13), 2102387
- [22] Cheng, D.; Wynn, T. A.; Wang, X.; Wang, S.; Zhang, M.; Shimizu, R.; Bai, S.; Nguyen, H.; Fang, C.; Kim, M.-c.et al. Unveiling the Stable Nature of the Solid Electrolyte Interphase between Lithium Metal and LiPON via Cryogenic Electron Microscopy, Joule 2020, 4 (11), 2484
- [23] Wang, J.; Huang, W.; Pei, A.; Li, Y.; Shi, F.; Yu, X.; Cui, Y. Improving Cyclability of Li Metal Batteries at Elevated Temperatures and its Origin Revealed by Cryo-electron Microscopy, Nature Energy 2019, 4 (8), 664
- [24] Devaux, D.; Harry, K. J.; Parkinson, D. Y.; Yuan, R.; Hallinan, D. T.; MacDowell, A. A.; Balsara, N. P. Failure Mode of Lithium Metal Batteries with a Block Copolymer Electrolyte Analyzed by X-Ray Microtomography, Journal of The Electrochemical Society 2015, 162 (7), A1301
- [25] Harry, K. J.; Hallinan, D. T.; Parkinson, D. Y.; MacDowell, A. A.; Balsara, N. P. Detection of Subsurface Structures Underneath Dendrites Formed on Cycled Lithium Metal Electrodes, Nature Materials 2014, 13 (1), 69
- [26] Harry, K. J.; Liao, X.; Parkinson, D. Y.; Minor, A. M.; Balsara, N. P. Electrochemical Deposition and Stripping Behavior of Lithium Metal across a Rigid Block Copolymer Electrolyte Membrane, Journal of The Electrochemical Society 2015, 162 (14), A2699
- [27] Maslyn, J. A.; Loo, W. S.; McEntush, K. D.; Oh, H. J.; Harry, K. J.; Parkinson, D. Y.; Balsara, N. P. Growth of Lithium Dendrites and Globules through a Solid Block Copolymer Electrolyte as a Function of Current Density, The Journal of Physical Chemistry C 2018, 122 (47), 26797
- [28] Maslyn, J. A.; Frenck, L.; Loo, W. S.; Parkinson, D. Y.; Balsara, N. P. Extended Cycling through Rigid Block Copolymer Electrolytes Enabled by Reducing Impurities in Lithium Metal Electrodes, ACS Applied Energy Materials 2019, 2 (11), 8197
- [29] Ho, A. S.; Barai, P.; Maslyn, J. A.; Frenck, L.; Loo, W. S.; Parkinson, D. Y.; Srinivasan, V.; Balsara, N. P. Uncovering the Relationship between Diameter and Height of Electrodeposited Lithium Protrusions in a Rigid Electrolyte, ACS Applied Energy Materials 2020, 3 (10), 9645
- [30] Maslyn, J. A.; McEntush, K. D.; Harry, K. J.; Frenck, L.; Loo, W. S.; Parkinson, D. Y.; Balsara, N. P. Preferential Stripping of a Lithium Protrusion Resulting in Recovery of a Planar Electrode, Journal of The Electrochemical Society 2020, 167 (10), 100553
- [31] Veeraraghavan, V. D.; Frenck, L.; Maslyn, J. A.; Loo, W. S.; Parkinson, D. Y.; Balsara, N. P. Evolution of Protrusions on Lithium Metal Anodes Stabilized by a Solid Block Copolymer Electrolyte Studied Using Time-Resolved X-ray Tomography, ACS Applied Materials & Interfaces 2021, 13 (23), 27006
- [32] Danzer, M. A. Generalized Distribution of Relaxation Times Analysis for the Characterization of Impedance Spectra, Batteries 2019, 5 (3), 53

- [33] Rosenbach, D.; Mödl, N.; Hahn, M.; Petry, J.; Danzer, M. A.; Thelakkat, M. Synthesis and Comparative Studies of Solvent-Free Brush Polymer Electrolytes for Lithium Batteries, ACS Applied Energy Materials 2019, 2 (5), 3373
- [34] Simon, F. J.; Hanauer, M.; Henss, A.; Richter, F. H.; Janek, J. Properties of the Interphase Formed between Argyrodite-Type Li6PS5Cl and Polymer-Based PEO10:LiTFSI, ACS Applied Materials & Interfaces 2019, 11 (45), 42186
- [35] Lennartz, P.; Borzutzki, K.; Winter, M.; Brunklaus, G. Viscoelastic Polyborosiloxanes as Artificial Solid Electrolyte Interphase on Lithium Metal Anodes, Electrochimica Acta 2021, 388, 138526
- [36] Borzutzki, K.; Winter, M.; Brunklaus, G. Improving the NMC111|Polymer Electrolyte Interface by Cathode Composition and Processing, Journal of The Electrochemical Society 2020, 167, 070546
- [37] Borzutzki, K.; Nair, J. R.; Winter, M.; Brunklaus, G. Does Cell Polarization Matter in Single-Ion Conducting Electrolytes?, ACS Applied Materials & Interfaces 2022, 14 (4), 5211
- [38] Ivers, T.; Eacute; E, E.; Weber, A.; eacute. Evaluation of Electrochemical Impedance Spectra by the Distribution of Relaxation Times, Journal of the Ceramic Society of Japan 2017, 125 (4), 193
- [39] Illig, J.; Schmidt, J. P.; Weiss, M.; Weber, A.; Ivers-Tiffée, E. Understanding the Impedance Spectrum of 18650 LiFePO4-Cells, Journal of Power Sources 2013, 239, 670
- [40] Pandolfi, R. J.; Allan, D. B.; Arenholz, E.; Barroso-Luque, L.; Campbell, S. I.; Caswell, T. A.; Blair, A.; De Carlo, F.; Fackler, S.; Fournier, A. P.et al. Xi-cam: A Versatile Interface for Data Visualization and Analysis, Journal of Synchrotron Radiation 2018, 25 (4), 1261
- [41] Hewlett, C. W. The Mass Absorption and Mass Scattering Coefficients for Homogeneous X Rays of Wave-Length between 0.13 and 1.05 Angstrom Units in Water, Lithium, Carbon, Nitrogen, Oxygen, Aluminum, and Iron, Physical Review 1921, 17 (3), 284
- [42] Groso, A.; Stampanoni, M.; Abela, R.; Schneider, P.; Linga, S.; Müller, R. Phase Contrast Tomography: An Alternative Approach, Applied Physics Letters 2006, 88 (21), 214104
- [43] Maia, F.; MacDowell, A.; Marchesini, S.; Padmore, H. A.; Parkinson, D. Y.; Pien, J.; Schirotzek, A.; Yang, C. Compressive Phase Contrast Tomography, ProcSPIE 2010, 7800, 1
- [44] Aurbach, D.; Zinigrad, E.; Cohen, Y.; Teller, H. A Short Review of Failure Mechanisms of Lithium Metal and Lithiated Graphite Anodes in Liquid Electrolyte Solutions, Solid State Ionics 2002, 148 (3), 405
- [45] Tikekar, M. D.; Choudhury, S.; Tu, Z.; Archer, L. A. Design Principles for Electrolytes and Interfaces for Stable Lithium-metal Batteries, Nature Energy 2016, 1 (9), 16114